Comprehensive study of the ultrafast photoexcited carrier dynamics in Sb_2Te_3–GeTe superlattices

Comprehensive study of the ultrafast photoexcited carrier dynamics in Sb_2Te_3–GeTe superlattices

Zhijiang Ye(叶之江)[1], Zuanming Jin(金钻明)[1,2,†], Yexin Jiang(蒋叶昕)[1], Qi Lu(卢琦)[3], Menghui Jia(贾梦辉)[5], Dong Qian(钱冬)[3,4], Xiamin Huang(黄夏敏)[6,7], Zhou Li(李舟)[6,7,8], Yan Peng(彭滟)[1,2], and Yiming Zhu(朱亦鸣)[1,2]

[1] *Terahertz Technology Innovation Research Institute, Terahertz Spectrum and Imaging Technology Cooperative Innovation Center, Shanghai Key Laboratory of Modern Optical System, University of Shanghai for Science and Technology, Shanghai* 200093, *China*
[2] *Shanghai Institute of Intelligent Science and Technology, Tongji University, Shanghai* 200092, *China*
[3] *Key Laboratory of Artificial Structures and Quantum Control (Ministry of Education), Shenyang National Laboratory for Materials Science, School of Physics and Astronomy, Shanghai Jiao Tong University, Shanghai* 200240, *China*
[4] *Tsung-Dao Lee Institute, Shanghai Jiao Tong University, Shanghai* 200240, *China*
[5] *State Key Laboratory of Precision Spectroscopy, East China Normal University, Shanghai* 200062, *China*
[6] *GBA Branch of Aerospace Information Research Institute, Chinese Academy of Sciences, Guangzhou* 510700, *China*
[7] *Guangdong Provincial Key Laboratory of Terahertz Quantum Electromagnetics, Guangzhou* 510700, *China*
[8] *University of Chinese Academy of Sciences, Beijing* 100039, *China*

(Received 18 April 2024; revised manuscript received 18 April 2024; accepted manuscript online 25 April 2024)

Chalcogenide superlattices Sb_2Te_3–GeTe is a candidate for interfacial phase-change memory (iPCM) data storage devices. By employing terahertz emission spectroscopy and the transient reflectance spectroscopy together, we investigate the ultrafast photoexcited carrier dynamics and current transients in Sb_2Te_3–GeTe superlattices. Sample orientation and excitation polarization dependences of the THz emission confirm that ultrafast thermo-electric, shift and injection currents contribute to the THz generation in Sb_2Te_3–GeTe superlattices. By decreasing the thickness and increasing the number of GeTe and Sb_2Te_3 layer, the interlayer coupling can be enhanced, which significantly reduces the contribution from circular photo-galvanic effect (CPGE). A photo-induced bleaching in the transient reflectance spectroscopy probed in the range of $\sim$ 1100 nm to $\sim$ 1400 nm further demonstrates a gapped state resulting from the interlayer coupling. These demonstrates play an important role in the development of iPCM-based high-speed optoelectronic devices.

Keywords: Sb_2Te_3/GeTe superlattices, ultrafast carrier dynamics, interfacial phase change memory, THz emission spectroscopy, transient reflectance spectroscopy

PACS: 42.65.Re, 73.21.Cd, 78.47.+q, 87.15.ht **DOI:** 10.1088/1674-1056/ad432a

1. Introduction

Chalcogenide superlattices Sb_2Te_3–GeTe, formed by alternately stacking Sb_2Te_3 layers with GeTe layers, are widely used in non-volatile data storage devices, such as interfacial phase-change memory (iPCM). Compared to phase change memories, the iPCM has the advantages of low switching energy, high-density memory, and long write–erase cycle lifetime.[1–6] Sb_2Te_3 is a typical three-dimensional topological insulator, featuring nontrivial gapless surface states.[7] GeTe is a narrow-bandgap semiconductor. It has been reported that the Sb_2Te_3–GeTe superlattices with inverted-Petrov phase are the Dirac semimetal.[8] The topological properties of Sb_2Te_3–GeTe are related to the geometry of the superlattice and are influenced by the Te–Ge–Ge–Te building unit.[1,9–13] The electronic structure of Sb_2Te_3–GeTe superlattices can be modified through applying electric fields or external stresses.[8,14] In addition, Sb_2Te_3–GeTe superlattices also exhibit the giant magnetoresistivity and multiferroic effects.[3,15]

Many optical measurements have been used to investigate the opto-electronic properties of the Sb_2Te_3–GeTe superlattices. For example, angle-resolved photoelectron spectroscopy has been employed to investigate the band structure of GeSbTe alloys.[16] Magneto-optical Kerr rotation and time-resolved optical Kerr measurements have been used to study the Dirac states and phase transition in Sb_2Te_3–GeTe.[17–19] Thermo-reflectance measurement has been employed to investigate the electrical and thermal transport characteristics of Sb_2Te_3–GeTe superlattices.[20] Optical pump–optical probe measurement has been utilized to probe the coherent phonon dynamics in Sb_2Te_3–GeTe superlattices.[21] The terahertz (THz) electric field has been used to induce the current signals in both multilayered Sb_2Te_3–GeTe and GeSbTe alloys.[22,23] We notice that the multilayered Sb_2Te_3–GeTe has the ability to produce THz radiation under optical excitation,[24] however, the mechanism has not been investigated in detail, which determines the potential applications of Sb_2Te_3–GeTe superlattices.

THz electromagnetic radiation has been used for broadband spectroscopic application in various fields.[25–27] On one hand, since the nonequilibrium distribution of photoexcited carriers causes the transient currents and subsequently generates the THz radiation,[28–30] THz emission spectroscopy has been proven to be a good method for investigating the transient

†Corresponding author. E-mail: physics_jzm@usst.edu.cn

carrier transport properties in symmetry-broken materials, such as ferromagnetic superlattices, transition metal dichalcogenides, strongly correlated and topological materials.[31–34] On the other hand, transient reflectance spectroscopy is a powerful technique to investigate bandgap renormalization, Pauli blocking and free carriers' absorption, providing an understanding of excited-state carrier dynamics in topological materials.[35,36]

In this paper, we combine THz emission spectroscopy and transient reflectance spectroscopy to investigate the ultrafast current and carrier dynamics in Sb_2Te_3–GeTe superlattices. Based on the incident angle, azimuth angle, and polarization dependences of THz emission measurements, we find that the thermo-electric current generated by the ultrafast laser-induced temperature gradient is the dominating ultrafast currents in Sb_2Te_3–GeTe superlattices. We also observe the shift current generated by the linear photo-galvanic effect (LPGE) and the injection current generated by the circular photo-galvanic effect (CPGE) in Sb_2Te_3–GeTe superlattices, which depend on the topological state with spin–momentum locking.[37–39] It can be found that, by decreasing the thickness of GeTe and Sb_2Te_3 layers, and increasing the number of GeTe and Sb_2Te_3 layers, the interlayer coupling can be enhanced, which significantly reduces the CPGE contribution. Further, utilizing transient reflectance spectroscopy, a photo-induced bleaching is observed at the wavelength of $\sim$ 1100 nm to $\sim$ 1400 nm, demonstrating a bandgap at $\sim$ 1.0 eV above the Fermi level. The interlayer coupling can undermine the topological state in Sb_2Te_3–GeTe superlattices. This explains why the injection current induced by CPGE is negligible in the multilayered Sb_2Te_3–GeTe sample. In this framework, the ultrafast current and carrier dynamics of Sb_2Te_3–GeTe superlattices add an essential piece to the fundamental properties and device applications of iPCM.

2. Sample preparation

Two types of Sb_2Te_3–GeTe samples were prepared in the experiments, as depicted in Figs. 1(a) and 1(b) for superlattices and bilayer samples, respectively. The molecular beam epitaxy (MBE) has been used to deposit GeTe and Sb_2Te_3 films on freshly cleaved mica substrates with ⟨001⟩ orientation. The thickness of each layer for the two samples is given in Figs. 1(a) and 1(b). We calculated the band structures of the Sb_2Te_3GeTe superlattices by using a first-principles method based on the density-functional theory (DFT).[40–43] As shown in Fig. 1(c), without spin–orbit coupling (SOC), the Sb_2Te_3–GeTe superlattices have a linear Diac-like energy band, similar to the Dirac semimetal. However, in the same calculation with SOC, the linear band opens and the bandgap appears at 0 eV and $\sim$ 1.0 eV, as shown in Fig. 1(d).

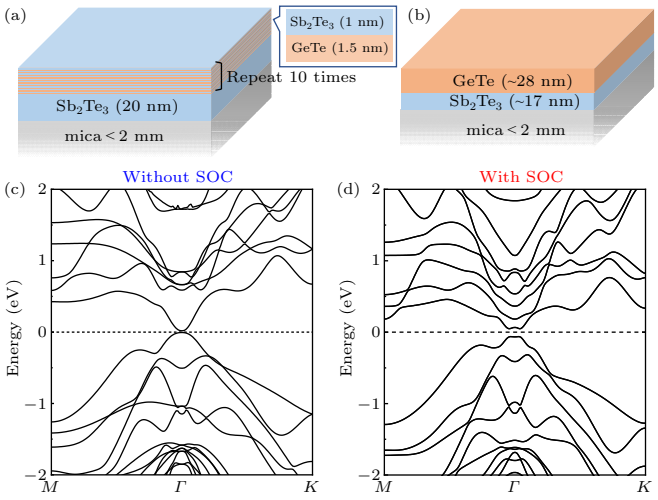

Fig. 1. The schematic diagram of (a) Sb_2Te_3–GeTe superlattices and (b) Sb_2Te_3–GeTe bilayer by stacking Sb_2Te_3 layers with GeTe layers. The calculated band structures of Sb_2Te_3–GeTe superlattices (c) without SOC and (d) with SOC.

3. Experimental setup

Figure 2(a) shows the schematic of THz emission spectroscopy. A Ti:sapphire laser (Solstice Ace, Spectra-Physics Inc) is used to generate laser pulses with a central wavelength of 800 nm, a repetition rate of 1 kHz, and a pulse duration of 35 fs. The output laser pulse is divided into pump and probe beams. The Sb_2Te_3–GeTe sample is photoexcited by the pump pulse. A half-wave plate (HWP) or a quarter-wave plate (QWP) is used to modulate the polarization state of the pump beam. The generated THz signal from the sample is focused onto a 1 mm thick ⟨110⟩-oriented ZnTe crystal for the electro–optical (EO) detection by a balanced photodetector. The emitted horizontally-polarized $E_{\mathrm{THz},x}$ and vertically-polarized $E_{\mathrm{THz},y}$ of the THz electric field are obtained by a pair of wire-grid polarizers.

In the transient reflectance spectroscopy, a Ti:sapphire femtosecond laser (Astrella, Coherent Inc) is used to generate laser pulses with a central wavelength of 800 nm, a repetition rate of 1 kHz, and a pulse width of 100 fs. The output laser pulse is split into two beams. One beam enters into an optical parametric amplifier (OPerA Solo, Coherent Inc) to generate different pump wavelengths. The other part of the pulse enters into a transient reflectance spectrometer (Helios, Ultrafast system). It is focused onto a sapphire plate to generate continuous probe wavelength. The pump beam and the probe beam are focused onto the sample at an incident angle of 54.7°. The probe beam, after being reflected by the sample, finally enters into the optical fiber detection. The spectral information at different time delays can be obtained by changing the time delay between the pump and the probe beams.

4. Experimental data analysis

Figure 2(b) shows the typical $E_{\mathrm{THz},x}$ from the Sb_2Te_3–GeTe superlattices illuminated by linearly polarized laser pulses at different incident angles $\theta = 0°$, $+45°$ and $-45°$ under pump fluence of 0.8 mJ/cm^2. The central frequency and bandwidth of the spectrum are approximately 0.23 THz and 0.29 THz, similar to the observation of 20-layer Sb_2Te_3–GeTe film by Makino *et al.*[24] If the surface depletion field was the mechanism of THz emission, as it is perpendicular to the sample surface, when θ is reversed from $+45°$ to $-45°$, the polarity of the THz pulse would be reversed. In addition, no THz emission can be detected when the sample is excited at normal incidence. However, it can be found that the waveform of the THz emission does not change when θ is changed from $+45°$ to $-45°$. Our observation demonstrates that the photo-induced ultrafast current follows parallel to the surface of the Sb_2Te_3–GeTe superlattices. Thus, the surface depletion field induced linear drift current can be excluded. Moreover, the wavevector independent THz emission confirms that the photon drag effect would not be the dominant mechanism for the THz emission in the Sb_2Te_3–GeTe superlattices.[37]

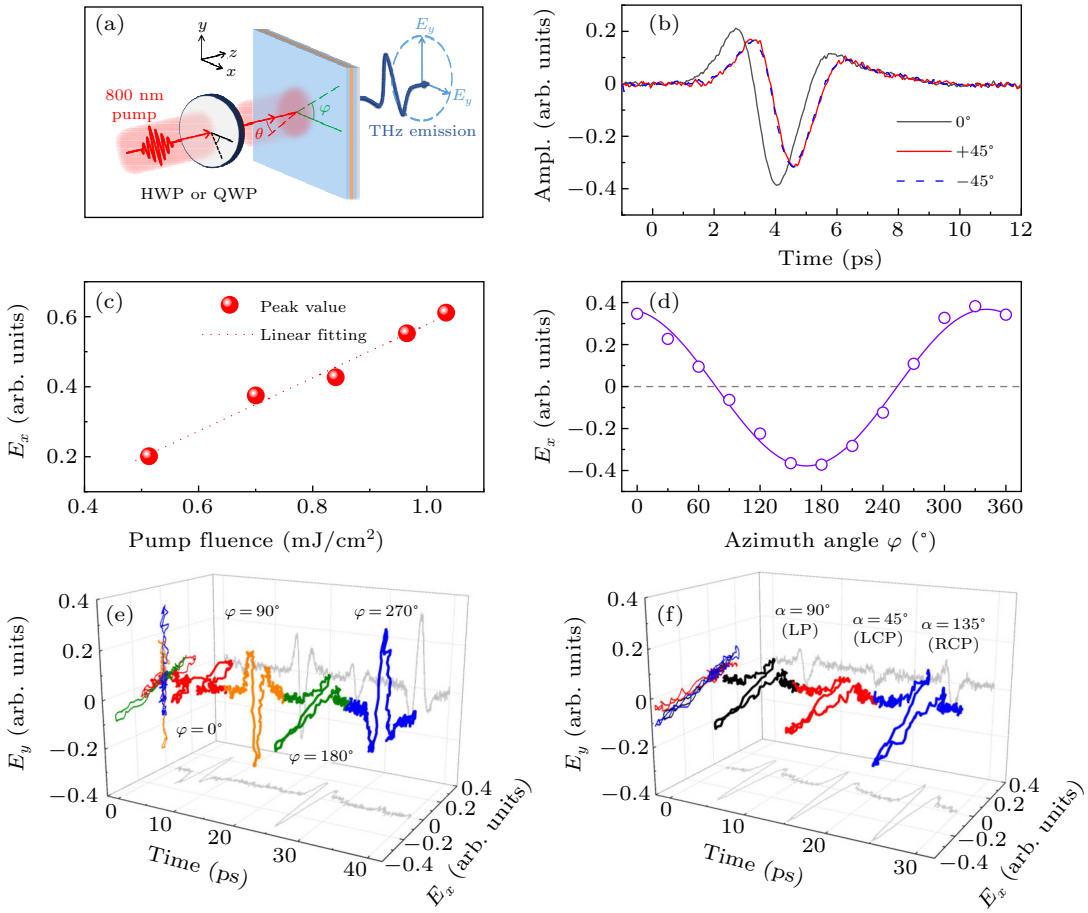

Fig. 2. Diagram of THz emission in a transmission measurement. (b) THz emission waveforms measured at incident angles $\theta = 0°$, $+45°$, $-45°$. Peak value of the horizontal component of THz emission as a function of (c) pump fluence and (d) azimuth angle φ. (e) The linearly polarized THz emission measured at $\varphi = 0°$, $90°$, $180°$, $270°$. (f) The linearly polarized THz emissions excited by left-handed, right-handed circularly and linearly polarized pump pulses. In panels (c)–(f), $\theta = 0°$.

As shown in Fig. 2(c), the peak amplitude of THz radiation $E_{\mathrm{THz},x}$ increases linearly with increasing pump fluence, indicating that the emitted THz signals are dominated by a second-order nonlinear effect. Figure 2(d) plots the peak amplitude of $E_{\mathrm{THz},x}$ as a function of azimuth angle φ, which exhibits a simple one-fold symmetry. The polarity of the $E_{\mathrm{THz},x}$ reverses when the φ is changed by 180°, which indicates that the emitted THz pulse is highly directional. Figure 2(e) shows that the polarization states of the emitted THz pulses rotate following φ. This experimental result agrees well with the cosine-like dependence of the peak amplitude (Fig. 2(d)). The direction of the ultrafast photocurrent follows the azimuthal angle φ of the Sb_2Te_3–GeTe superlattices. Figure 2(f) shows the THz emission excited by different polarized pump beams. The *y*-polarized THz electric field component is undetectable compared to the *x*-polarized component, which indicates the linearly polarized THz radiation. The polarization and intensity are almost equal for linearly, left and right circularly polarized excitations.

Owing to the MBE-grown Sb_2Te_3–GeTe superlattices,

such layered stacking is lacking the space-inversion symmetry. The optical transitions induced by linearly polarized laser pulse give rise to a photocurrent in materials with low spatial symmetry. Therefore, both linear and nonlinear optical processes can induce ultrafast photocurrent for THz emission.[44,45] The nonlinear photocurrent enables a probe of topological state.[46,47] In order to elucidate the nonlinear optical process of THz emission from the Sb_2Te_3–GeTe superlattices, we investigate the THz amplitude with respect to a periodic polarization modulation of the pump pulse at the normal incidence ($\theta = 0°$). In this configuration, the photon-drag THz emission mechanism can be nearly excluded.

Figure 3(a) shows the THz emissions from Sb_2Te_3–GeTe superlattices for various linearly pump polarizations. The dependences of the peak amplitude of THz emission from Sb_2Te_3–GeTe superlattices and Sb_2Te_3–GeTe bilayer on the linear-polarization angle β are shown in Figs. 3(b) and 3(c), respectively. The polarization dependent peak amplitude of the THz radiation can be fitted well by $\cos 2\beta$, which is consist with the shift current mechanism.[37,39]

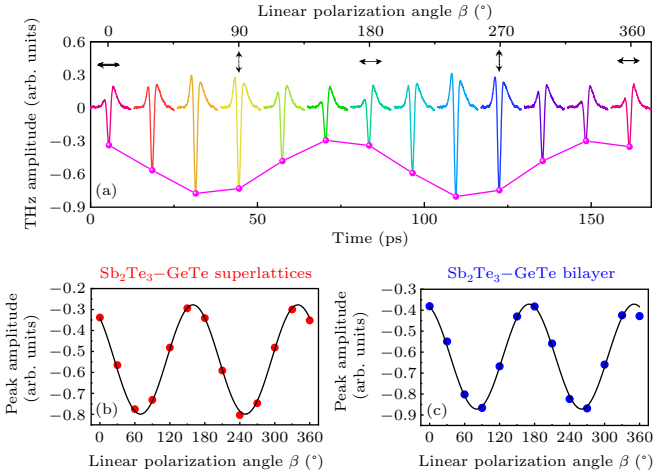

Fig. 3. (a) THz emission from Sb_2Te_3–GeTe superlattices measured at various pump polarization states by rotating the HWP, characterized by the angle β. The peak values of THz EO signals for (b) Sb_2Te_3–GeTe superlattices and (c) Sb_2Te_3–GeTe bilayer as functions of β, respectively.

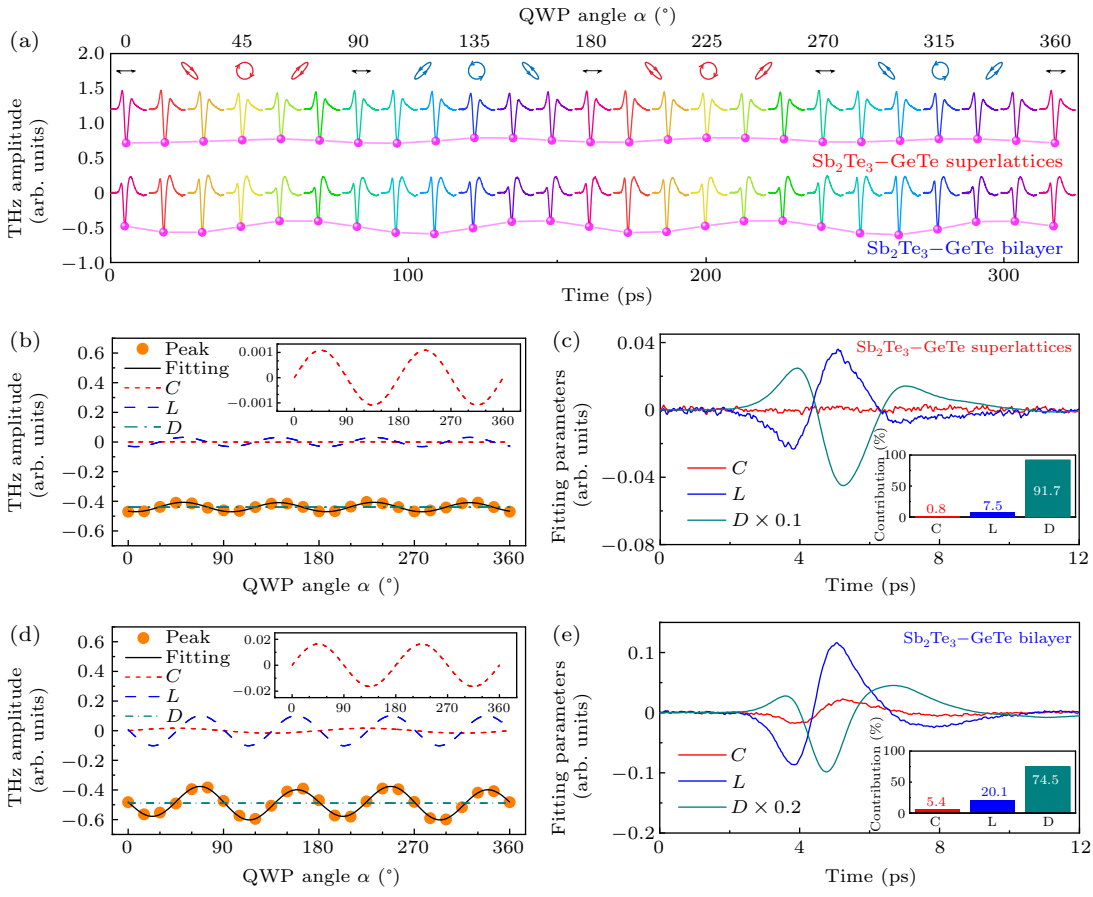

Fig. 4. (a) THz emission from Sb_2Te_3–GeTe superlattices and Sb_2Te_3–GeTe bilayer under different polarized pumping at various QWP angle α. For clarity, the THz waveforms are shifted horizontally. The peak amplitude of THz electric field dependent on α for (b) Sb_2Te_3–GeTe superlattices and (d) Sb_2Te_3–GeTe bilayer. The orange circles and black lines represent the experimental data and fitting result by Eq. (1). (c) and (e) Time-dependent fitting parameters of $C(t)$, $L(t)$, and $D(t)$ for Sb_2Te_3–GeTe superlattices and bilayer samples, respectively. The inset represents the weight of contribution from CPGE, LPGE and polarization-independent thermo-electric current.

Figure 4(a) shows the THz emissions from Sb_2Te_3–GeTe superlattices and Sb_2Te_3–GeTe bilayer under various pump polarizations tuned from linear to circular by rotating the QWP from 0° to 360°, at $\varphi = 180°$ and $\theta = 0$. In Figs. 4(b) and 4(d), the pump polarization dependent THz peak amplitudes measured at $t = 5.3$ ps (orange circles) indicate a superposition of

different processes, which can be fitted by the phenomenological expression[45,48–50]

$$E_{\mathrm{THz},x}(\alpha,t) = C_x(t)\sin(2\alpha) + L_x(t)\sin(4\alpha+\alpha_0) + D_x(t), \quad (1)$$

where α is the angle of the QWP. The first term represents the helicity-dependent THz emission. The coefficient $C(t)$ parameterizes the injection current induced by circularly polarized light through CPGE, which is dependent on photoexcited spin dynamics and topological states.[51] The second term describes the linear-polarization-dependent THz emission. The coefficient $L(t)$ parameterizes the shift current induced by linearly polarized light via LPGE. The third term describes the polarization-independent THz emission, the coefficient $D(t)$ represents ultrafast thermo-electric current due to a laser-induced temperature gradient in the thermoelectric materials.[45,52]

As shown in Figs. 4(b) and 4(d), the solid lines are the fitting curve using Eq. (1), and the dashed and the dotted lines indicate the L ($t = 5.3$ ps) and D ($t = 5.3$ ps), respectively. The insets of Figs. 4(b) and 4(d) highlight the contributions of C ($t = 5.3$ ps) following 2α. D ($t = 5.3$ ps) is unrelated to the polarization of light, as shown by a large offset. This method can be extended to the entire time-domain, ranging from 0 ps to 13 ps. Figures 4(c) and 4(e) show the time-dependent parameters of $C(t)$, $L(t)$, and $D(t)$ by fitting the amplitude of $E_{\mathrm{THz},x}(\alpha,t)$ for Sb_2Te_3–GeTe superlattices and bilayer sample, respectively. We can distinguish different mechanisms of the oscillating transient currents for THz emission. By integrating the $C(t)$, $L(t)$, and $D(t)$, the insets of Figs. 4(c) and 4(e) show the proportion of $C = 0.8\%$, $L = 7.5\%$, and $D = 91.7\%$ for Sb_2Te_3–GeTe superlattices and $C = 5.4\%$, $L = 20.1\%$, and $D = 74.5\%$ for the bilayer sample.

It can be seen that D is much larger than C and L, indicating that the polarization-independent thermo-electric current governs the THz radiation. LPGE generates a shift current during the optical excitation between the initial and final states of different charge centers, which has a geometrical origin that is described by the Berry phase connection.[53,54] For the CPGE, photons in circularly polarized light couple with the spin of electrons by providing a defined angular momentum. The coupling is strong in topological materials because of the spin–momentum locking feature of topological state.[55] As a comparison, it can be found that C decreases from 5.4% (bilayer sample) to 0.8% (multilayer superlattices), which indicates that the larger interlayer coupling enables the Sb_2Te_3–GeTe superlattices to present less topological state, which makes the CPGE less observable. It is consistent with the observation that difference of THz emission from Sb_2Te_3–GeTe superlattices excited by left-handed and right-handed pump laser is negligible in Fig. 2(f).

Finally, we perform the time-resolved reflectance spectroscopy to further investigate the relaxation dynamics of excited-state carriers in Sb_2Te_3–GeTe superlattices. The laser pulse with 800 nm serves as a pump. Figures 5(a) and 5(b) depict the 2D contour plots of transient differential reflectance (ΔR) in the visible range of 450 nm–750 nm and the near-infrared range of 850 nm–1550 nm. The x axis and y axis show the probe wavelength and probe delay, respectively. Figure 5(c) shows the kinetic curves of $\Delta R(\Delta t)$ at various probe wavelengths, the non-oscillatory carrier relaxation process is superimposed on a coherent oscillation. A phenomenology model can be used to fit the kinetic profiles

$$\Delta R(\Delta t) = a_1 \mathrm{e}^{-\frac{\Delta t}{t_1}} + b_1 \mathrm{e}^{-\frac{\Delta t}{t_2}} \times \cos(2\pi f \Delta t + \phi_0) + c_1, \quad (2)$$

where Δt is the pump-to-probe time delay. The first term describes the relaxation of the excited carriers. t_1 denotes the decay time that characterizes the non-oscillatory carrier relaxation. The second term represents a damped coherent oscillation. f and t_2 represent the frequency and decay time of the coherent oscillation, respectively. The fitting is given in Fig. 5(c). The extracted t_1 is much longer than the time window used. The oscillation frequency locates in a range of $\sim$ 30–60 GHz, as given in Fig. 5(c), which could be attributed to the coherent acoustic phonon. In addition, the extracted t_2 is in a range of $\sim$ 5 ps–10 ps.

As seen in Fig. 5(a), the positive ΔR represents the photo-induced absorption (PIA), which covers the ranges of 450 nm–750 nm and 850 nm–1600 nm. It signifies prominent optically allowed transitions from the first valence band (VB_1) to the second conduction band (CB_2) in the Sb_2Te_3–GeTe superlattices, as shown in Fig. 5(d). In Fig. 5(b), a negative ΔR peak in the near-infrared range (from $\sim$ 1100 nm to $\sim$ 1400 nm) can be found, which demonstrates the transition from the first gapped state (GS_1) to the second gapped state (GS_2), as shown in Fig. 5(d). Upon photoexcitation from the ground state to the excited state, the carriers are pumped into CB_2 ($\sim$ 1.4 eV). And then, the carriers relax to the bottom of CB_2 through interband relaxation pathways, which causes an increase of the carrier population. The level of GS_2 becomes a metastable state, leading to the ground-state bleaching (GSB). Thus, the negative ΔR signal observed at $\sim$ 1100 nm to $\sim$ 1400 nm is aligned with the energy level of GS_2 about $\sim$ 1.0 eV. As proposed by optical Kerr effect and electronic transport measurements, the interlayer coupling between Sb_2Te_3 and GeTe layers within the Sb_2Te_3–GeTe superlattices would undermine the topological state, especially in the interfaces.[18,56,57] It leads to the broken linear band dispersion. And then the gapped state between CB_2 and VB_2 appears, which is consistent with the band structure calculation with SOC in Fig. 1(d). The gapped state makes it easier for carrier population to accumulate in the GS_2, resulting in the appearance of photo-induced bleaching

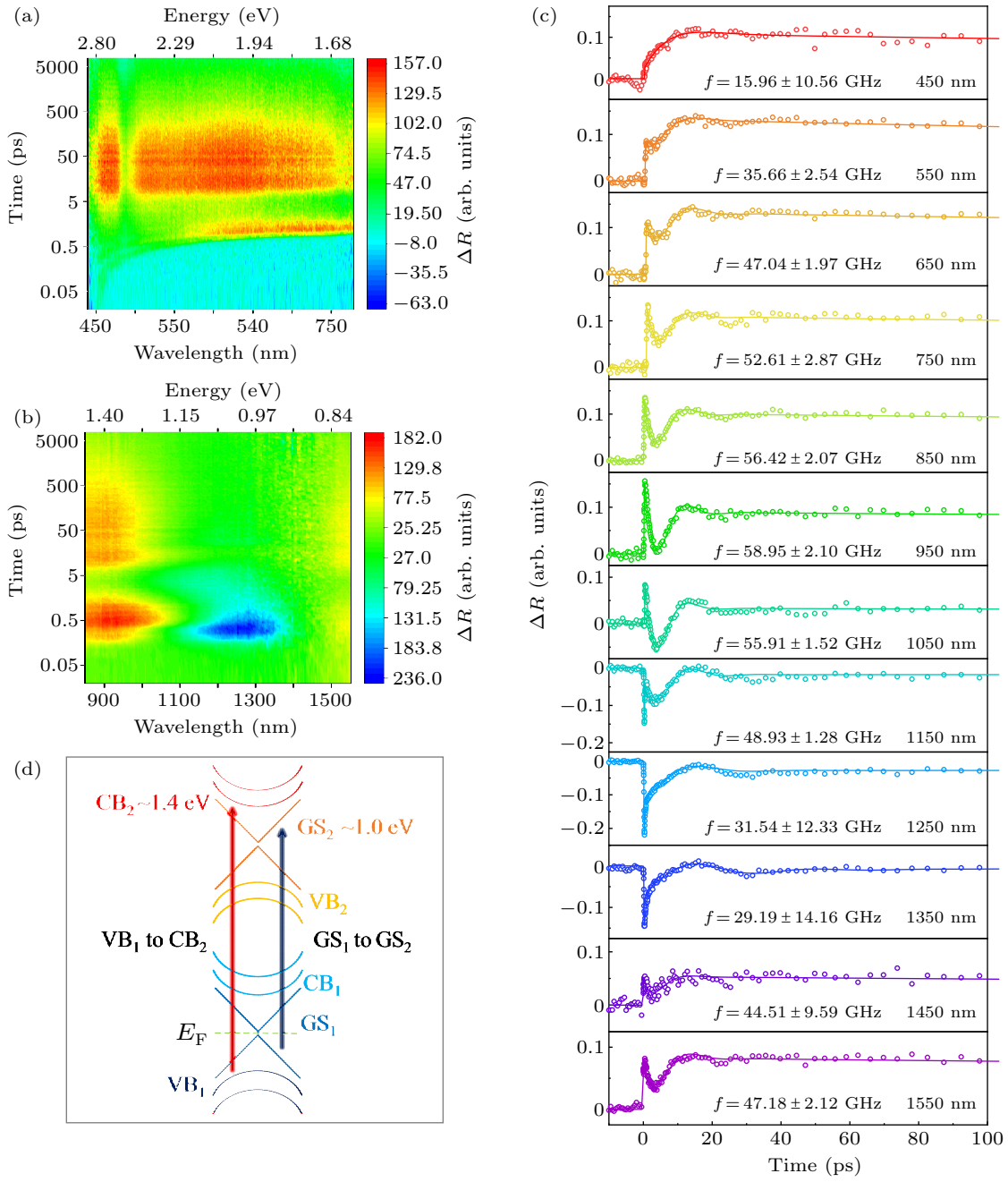

Fig. 5. (a) and (b) The 2D contour plots of ΔR in the Sb_2Te_3–GeTe superlattices excited with 1.55 eV, and probed in the visible and near-infrared range. (c) The time-revolved ΔR at different probe wavelengths with fitting by Eq. (2). (d) The schematic diagram describes an optically allowed transitions from VB_1 to CB_2 (red arrow) and from GS_1 to GS_2 (blue arrow), the energy band structure is based on calculation with SOC.

at $\sim$ 1.0 eV. The interlayer coupling changes the linear energy band and generates the gapped state, thus the topological state is expected to be suppressed largely, which explains why the injection current via CPGE is negligible for THz emission in Sb_2Te_3–GeTe superlattices.

5. Summary

In summary, we distinguish the different ultrafast photocurrents driven by thermoelectric effect, linear photo-galvanic effect and circular photo-galvanic effect. The time-resolved reflectance spectroscopy visualizes the excited-state carrier relaxation of Sb_2Te_3–GeTe superlattices. The photo-induced bleaching and negligible circular photo-galvanic effect in Sb_2Te_3–GeTe superlattices signify the gapped state which may come from interlayer coupling. Our result could play an important role in the development of iPCM-based high-speed optoelectronic devices.

Acknowledgments

Project supported by the National Key Research and Development Program of China (Grant Nos. 2023YFF0719200 and 2022YFA1404004), the National Natural Science Foundation of China (Grant Nos. 62322115, 61988102, 61975110, 62335012, and 12074248), 111 Project (Grant

No. D18014), the Key Project supported by Science and Technology Commission Shanghai Municipality (Grant No. YDZX20193100004960), Science and Technology Commission of Shanghai Municipality (Grant Nos. 22JC1400200 and 21S31907400), and General Administration of Customs People's Republic of China (Grant No. 2019HK006).

References

[1] Simpson R E, Fons P, Kolobov A V, Fukaya T, Krbal M, Yagi T and Tominaga J 2011 *Nat. Nanotechnol.* **6** 501
[2] Okabe K L, Sood A, Yalon E, Neumann C M, Asheghi M, Pop E, Goodson K E and Wong H S P 2019 *J. Appl. Phys.* **125** 184501
[3] Tominaga J, Simpson R E, Fons P and Kolobov A V 2011 *Appl. Phys. Lett.* **99** 152105
[4] Egami T, Johguchi K, Yamazaki S and Takeuchi K 2014 *Jpn. J. Appl. Phys.* **53** 04ED02
[5] Ohyanagi T and Takaura N 2016 *AIP Advances* **6** 105104
[6] Sa B, Zhou J, Sun Z, Tominaga J and Ahuja R 2012 *Phys. Rev. Lett.* **109** 096802
[7] Zhu S, Ishida Y, Kuroda K, Sumida K, Ye M, Wang J, Pan H, Taniguchi M, Qiao S, Shin S and Kimura A 2015 *Scientific Reports* **5** 13213
[8] Tominaga J, Kolobov A V, Fons P, Nakano T and Murakami S 2014 *Advanced Materials Interfaces* **1** 1300027
[9] Di Sante D, Barone P, Bertacco R and Picozzi S 2013 *Adv. Mater.* **25** 509
[10] Ohyanagi T, Kitamura M, Araidai M, Kato S, Takaura N and Shiraishi K 2014 *Appl. Phys. Lett.* **104** 252106
[11] Kolobov A V, Fons P, Saito Y and Tominaga J 2017 *ACS Omega* **2** 6223
[12] Momand J, Wang R, Boschker J E, Verheijen M A, Calarco R and Kooi B J 2015 *Nanoscale* **7** 19136
[13] Kim J, Kim J, Kim K-S and Jhi S-H 2012 *Phys. Rev. Lett.* **109** 146601
[14] Saito Y, Makino K, Fons P, Kolobov A V and Tominaga J 2017 *ACS Applied Materials & Interfaces* **9** 23918
[15] Tominaga J, Kolobov A V, Fons P J, Wang X, Saito Y, Nakano T, Hase M, Murakami S, Herfort J and Takagaki Y 2015 *Science and Technology of Advanced Materials* **16** 014402
[16] Kellner J, Bihlmayer G, Liebmann M, Otto S, Pauly C, Boschker J E, Bragaglia V, Cecchi S, Wang R N, Deringer V L, Küppers P, Bhaskar P, Golias E, Sánchez-Barriga J, Dronskowski R, Fauster T, Rader O, Calarco R and Morgenstern M 2018 *Communications Physics* **1** 5
[17] Bang D, Awano H, Tominaga J, Kolobov A V, Fons P, Saito Y, Makino K, Nakano T, Hase M, Takagaki Y, Giussani A, Calarco R and Murakami S 2014 *Scientific Reports* **4** 5727
[18] Mondal R, Aihara Y, Saito Y, Fons P, Kolobov A V, Tominaga J and Hase M 2018 *ACS Applied Materials & Interfaces* **10** 26781
[19] Suzuki T, Mondal R, Saito Y, Fons P, Kolobov A V, Tominaga J, Shigekawa H and Hase M 2019 *J. Phys.: Condens. Matter* **31** 415502
[20] Kwon H, Khan A I, Perez C, Asheghi M, Pop E and Goodson K E 2021 *Nano Lett.* **21** 5984
[21] Makino K, Saito Y, Fons P, Kolobov A V, Nakano T, Tominaga J and Hase M 2016 *Scientific Reports* **6** 19758
[22] Shu M J, Zalden P, Chen F, Weems B, Chatzakis I, Xiong F, Jeyasingh R, Hoffmann M C, Pop E, Philip Wong H S, Wuttig M and Lindenberg A M 2014 *Appl. Phys. Lett.* **104** 251907
[23] Makino K, Kuromiya S, Takano K, Kato K, Nakajima M, Saito Y, Tominaga J, Iida H, Kinoshita M and Nakano T 2016 *ACS Applied Materials & Interfaces* **8** 32408
[24] Makino K, Kato K, Saito Y, Fons P, Kolobov A V, Tominaga J, Nakano T and Nakajima M 2019 *Opt. Lett.* **44** 1355
[25] Zhu Y, Zang X, Chi H, Zhou Y, Zhu Y and Zhuang S 2023 *Light: Advanced Manufacturing* **4** 9
[26] Lyu J, Shen S, Chen L, Zhu Y and Zhuang S 2023 *PhotoniX* **4** 28
[27] Peng Y, Huang J, Luo J, Yang Z, Wang L, Wu X, Zang X, Yu C, Gu M, Hu Q, Zhang X, Zhu Y and Zhuang S 2021 *PhotoniX* **2** 12
[28] Peng Q, Peng Z, Lang Y, Zhu Y, Zhang D, Lü Z and Zhao Z 2022 *Chin. Phys. Lett.* **39** 053301
[29] Jia G R, Zhao D X, Zhang S S, Yue Z W, Qin C C, Jiao Z Y and Bian X B 2023 *Chin. Phys. Lett.* **40** 103202
[30] Wu X 2023 *Chin. Phys. Lett.* **40** 054001
[31] Pettine J, Padmanabhan P, Sirica N, Prasankumar R P, Taylor A J and Chen H T 2023 *Light: Science & Applications* **12** 133
[32] Jin Z, Peng Y, Ni Y, Wu G, Ji B, Wu X, Zhang Z, Ma G, Zhang C, Chen L, Balakin A V, Shkurinov A P, Zhu Y and Zhuang S 2022 *Laser & Photonics Reviews* **16** 2100688
[33] Jin Z, Guo Y, Peng Y, Zhang Z, Pang J, Zhang Z, Liu F, Ye B, Jiang Y, Ma G, Zhang C, Balakin A V, Shkurinov A P, Zhu Y and Zhuang S 2023 *Advanced Physics Research* **2** 2200049
[34] Lan Z, Li Z, Xu H, Liu F, Jin Z, Peng Y and Zhu Y 2024 *Chin. Phys. Lett.* **41** 044203
[35] Glinka Y D, Li J, He T and Sun X W 2021 *ACS Photonics* **8** 1191
[36] Sharma P, Bhardwaj A, Sharma R, Awana V P S, Narayanan T N, Raman K V and Kumar M 2022 *The Journal of Physical Chemistry C* **126** 11138
[37] Yang S, Cheng L and Qi J 2023 *Ultrafast Science* **3** 0047
[38] Tong M, Hu Y, He W, Yu X L, Hu S, Cheng X and Jiang T 2021 *ACS Nano* **15** 17565
[39] Gao Y, Pei Y, Xiang T, Cheng L and Qi J 2022 *iScience* **25** 104511
[40] Grimme S 2006 *Journal of Computational Chemistry* **27** 1787
[41] Blochl P E 1994 *Phys. Rev. B* **50** 17953
[42] Perdew J P, Burke K and Ernzerhof M 1996 *Phys. Rev. Lett.* **77** 3865
[43] Kresse G and Joubert D 1999 *Phys. Rev. B* **59** 1758
[44] Xu X, Huang Y, Zhang Z, Liu J, Lou J, Gao M, Wu S, Fang G, Zhao Z, Chen Y, Sheng Z and Chang C 2023 *Chin. Phys. Lett.* **40** 045201
[45] Boland J L, Damry D A, Xia C Q, Schönherr P, Prabhakaran D, Herz L M, Hesjedal T and Johnston M B 2023 *ACS Photonics* **10** 1473
[46] Seifert P, Vaklinova K, Kern K, Burghard M and Holleitner A 2017 *Nano Lett.* **17** 973
[47] Tong M, Hu Y, Wang Z, Zhou T, Xie X, Cheng X and Jiang T 2021 *Nano Lett.* **21** 60
[48] Gao Y, Kaushik S, Philip E J, Li Z, Qin Y, Liu Y P, Zhang W L, Su Y L, Chen X, Weng H, Kharzeev D E, Liu M K and Qi J 2020 *Nat. Commun.* **11** 720
[49] Ji Z, Liu G, Addison Z, Liu W, Yu P, Gao H, Liu Z, Rappe A M, Kane C L, Mele E J and Agarwal R 2019 *Nat. Mater.* **18** 955
[50] McIver J W, Hsieh D, Steinberg H, Jarillo-Herrero P and Gedik N 2012 *Nat. Nanotechnol.* **7** 96
[51] Hosur P 2011 *Phys. Rev. B* **83** 035309
[52] Fu C, Sun Y and Felser C 2020 *APL Materials* **8** 040913
[53] Tan L Z, Zheng F, Young S M, Wang F, Liu S and Rappe A M 2016 *npj Computational Materials* **2** 16026
[54] Osterhoudt G B, Diebel L K, Gray M J, Yang X, Stanco J, Huang X, Shen B, Ni N, Moll P J W, Ran Y and Burch K S 2019 *Nat. Mater.* **18** 471
[55] Ruan S, Lin X, Chen H, Song B, Dai Y, Yan X, Jin Z, Ma G and Yao J 2021 *Appl. Phys. Lett.* **118** 011102
[56] Nguyen T A, Backes D, Singh A, Mansell R, Barnes C, Ritchie D A, Mussler G, Lanius M, Grützmacher D and Narayan V 2016 *Scientific Reports* **6** 27716
[57] Nakamura H, Hofmann J, Inoue N, Koelling S, Koenraad P M, Mussler G, Grützmacher D and Narayan V 2020 *Scientific Reports* **10** 21806